LAWRENCE
LIVERMORE
NATIONAL
LABORATORY

LLNL-JRNL-778865

High-yield growth kinetics and spatial mapping of single-walled carbon nanotube forests at wafer scale

E. R. Meshot, S. J. Park, S. F. Buchsbaum, M. L. Jue, T. R. Kuykendall, E. Schaible, L. B. B. Aji, S. O. Kucheyev, K. J. J. Wu, F. Fornasiero

June 21, 2019

Carbon

Disclaimer

LLNL-JRNL-778865

High-yield growth kinetics and spatial mapping of single-walled carbon nanotube forests at wafer scale

Eric R. Meshot,[1] Sei Jin Park,[1] Steven F. Buchsbaum,[1] Melinda L. Jue,[1] Tevye R. Kuykendall,[2] Eric Schaible,[3] Leonardus Bimo Bayu Aji,[1] Sergei O. Kucheyev,[1] Kuang Jen J. Wu,[1] Francesco Fornasiero[1,]*

[1]Physical and Life Sciences Directorate, Lawrence Livermore National Laboratory, 7000 East Avenue, Livermore, California 94550 USA

[2]Molecular Foundry, Lawrence Berkeley National Laboratory, 1 Cyclotron Road, Berkeley, California 94720

[3]Advanced Light Source, Lawrence Berkeley National Laboratory, 1 Cyclotron Road, Berkeley, California 94720

*Corresponding author email: fornasiero1@llnl.gov

ABSTRACT

Emerging commercial applications of vertically aligned, single-walled carbon nanotube (SWCNT) "forests" require synthesis that minimizes nanotube diameter while maximizing number density across substrate areas exceeding centimeter scale. To address this need, we synthesized SWCNT forests on full silicon wafers with notable reproducibility and uniformity, and co-optimized growth for small *diameters* and high *densities* across large *areas* to access new territory in this 3D parameter space. We mapped the spatial uniformity of key structural features using Raman microscopy, synchrotron X-ray scattering, and Rutherford backscattering spectrometry. Low C_2H_2 flux over sub-nm Fe/Mo catalysts produced small-diameter SWCNTs (2.1 nm) at high number densities (2.26×10^{12} cm^{-2}) on wafers up to 6 in. Although removing Mo resulted in larger SWCNT diameters and lower densities ($< 0.7 \times 10^{12}$ cm^{-2}), mass conversion rates from C_2H_2 to SWCNT product were high and remarkably invariant for catalyst compositions and densities (i.e., 47.7% or 1.30×10^{6} % g-$catalyst^{-1}$ on 4-in. wafers). These carbon conversion efficiencies far exceed typical benchtop reactors and are on par with the best reported literature values. Our detailed elucidation of correlations among structural characteristics within this resource-efficient process is expected to guide future scale-up efforts of SWCNT forest growth beyond wafer scale.

TEXT

1. Introduction

Individual single-walled carbon nanotubes (SWCNT) possess a compelling combination of high thermal, electrical, and fluidic conductivities, high specific strength, as well as the presence of an electronic band gap in certain types. Driven by these exciting constituent properties, commercial applications of vertically aligned "forests" are on the horizon, with the emergence of their use as electronic interconnects [1, 2], electron emitters [3, 4], optical absorbers [5], terahertz devices [6, 7] [8], optical rectennas [9], thermal interface materials [10-12], gecko-inspired dry adhesives [13], mechanical dampers [14, 15], selective membrane nanochannels [16-19], and advanced yarns and sheets [20, 21].

Despite these promising demonstrations, realizing a tangible impact on mainstream applications is critically limited by the inability to synthesize large-area SWCNT forests with high reproducibility and uniformity in both their growth kinetics and structural characteristics. Addressing this challenge requires transition from conventional benchtop reactors toward larger ones, which can significantly change the growth environment, whereby simply scaling recipes may not suffice. Instead, this transition demands detailed mechanistic understanding of the governing rules that couple key structural features of SWCNTs (i.e., diameter, density, length, graphitization, etc.) along with their temporal and spatial evolution. Large-area SWCNT forests with high densities and small diameters are especially important for a majority of the applications listed above, yet they are conspicuously absent from the reported literature (**Figure 1**).

Indeed, researchers have made progress over the past decade in scaling synthesis of SWCNT forests to large areas beyond the "chip scale". Wyss, et al. [22], for example, reported

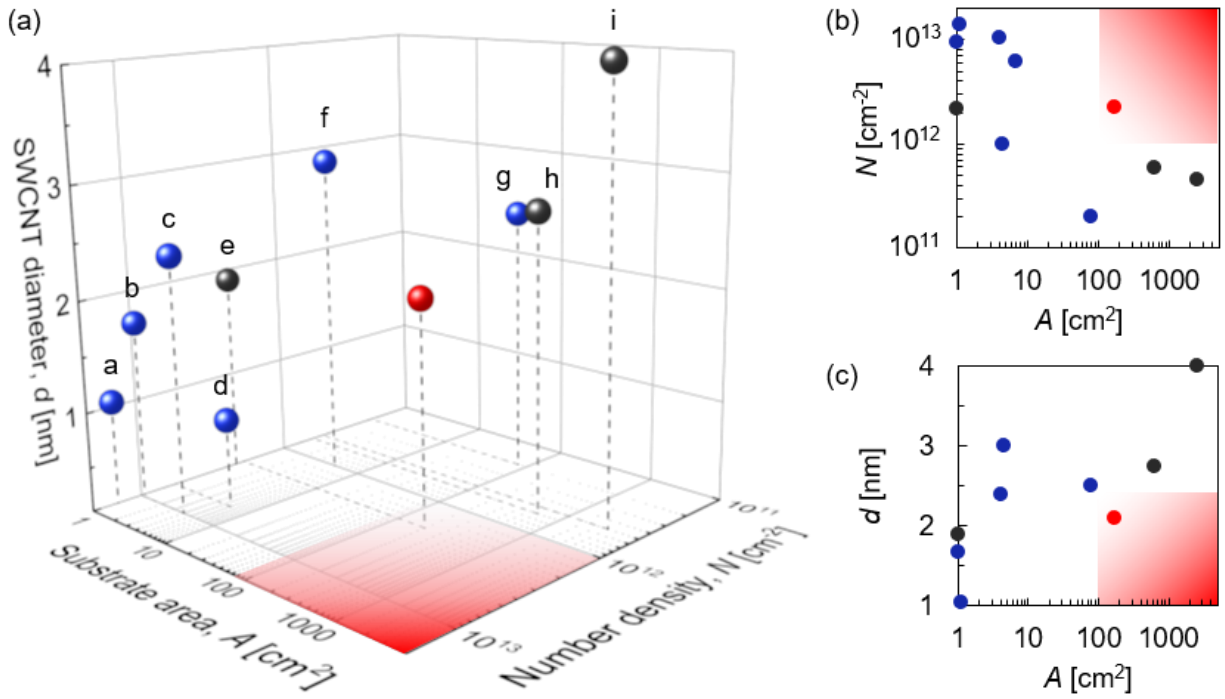

Figure 1. (a) 3D parameter space for SWCNT forest growth (axes = SWCNT diameter, number density, and substrate area). The red point indicates this work, while the other data points are taken from the literature: (a) [23], (b) [24], (c) [25], (d) [26], (e) [27], (f) [28], (g) [22], (h) [29], (i) [30]. Red shaded region represents currently unattained parameter space, required for enabling applications. Blue data points: growth on Si substrates; grey points: growth on metal foils. 2D projections: (b) number density and (c) SWCNT diameter plotted against substrate area.

growth on 4-in. Si wafers, and Yasuda, et al. [29] demonstrated growth on 21.0 × 29.7 cm^2 metal foils. More recently, a commercial SWCNT forest plant based on the latter work extended the growth area to 50 × 50 cm^2 metal substrates [30]. However, these processes relied on Fe-only catalyst layers to optimize for yield (i.e., SWCNT lengthening rate), so CNT densities remained relatively low (~10^{11} cm^{-2}) and diameters large (~4 nm). In contrast, the highest densities (~10^{13} cm^{-2}) [23] and smallest mean diameter (0.9 nm) [26] reported so far were achieved with bi-metallic catalysts. These benchmark forest features have only been demonstrated on ~1 cm^2 chips and, in some cases, with terminal forest heights too short (i.e., < 10 μm) for a broad range of applications. The challenge of demonstrating reproducible and uniform growth of dense SWCNT forests on large areas is exacerbated by the lack of information regarding how key structural features vary over multiple growth runs and across large substrates.

In this study, we achieved reproducible and uniform synthesis of SWCNT forests on full silicon wafers by low-pressure chemical vapor deposition (CVD) using an Fe/Mo thin-film catalyst. We leveraged a suite of advanced characterization techniques to generate area maps across wafers and quantitatively evaluate the uniformity of various key structural features, including forest height, graphitization, and diameters by Raman microscopy; mean diameter and wall number by synchrotron X-ray scattering; and forest density by Rutherford backscattering spectrometry (RBS). We validated the reproducibility of our process on 4-in. wafers by confirming high uniformity in forest structural features, both for multiple sequential growths as well as across the entire wafer from a single growth run. To our knowledge, this work represents the best co-optimization of SWCNT diameter, density, and area (**Figure 1**). Furthermore, we showed that the combination of low C_2H_2 flux over sub-nm Fe/Mo catalyst films produced small-diameter SWCNTs (mean of 2.1 nm) with average number densities up to 2.26 x 10^{12} cm^{-2},

while maintaining exceptional carbon conversion efficiency on 4- and 6-in. wafers (~48% and 61%, respectively). We provided visual and statistical evidence via TEM that the addition of Mo to Fe induced the formation of smaller, more closely packed particles, which was critical to large-area growth of dense, small-diameter SWCNT forests. Remarkably, we demonstrated constant mass kinetics and catalyst lifetime that were invariant with catalyst composition and SWCNT density. As a consequence, we revealed a pronounced inverse correlation between forest height kinetics and SWCNT number density. Together with the linear scaling of forest height with growth time, these results hint at growth kinetics limited by gas-phase processes. Finally, we derived an analytical relationship between the SWCNT lengthening rate and forest density, which explains our experimental data well and provides insight for tuning structural features and scaling up growth.

2. Results and Discussion

2.1 Serial repeatability

Previous literature has analyzed reproducibility of CNT forest growth yield and density on small substrates [31-33], yet to our knowledge there are no detailed reports on the consistency of SWCNT forests at wafer scale. To evaluate the run-to-run reproducibility of wafer-scale SWCNT forest synthesis, we performed five growths in series on 4-in. wafers (**Figure 2a**) in an AIXTRON® Black Magic cold-wall, low-pressure CVD system. For these consecutive growths, we deposited thin films of Fe/Mo/Al_2O_3 (5.5/0.5/400 Å) multilayer catalysts during the same electron-beam evaporation run. Achieving repeatable and uniform SWCNT forest growth at wafer scale required first establishing an optimal window of H_2O concentrations (~120-250 ppm_v) (**Figure S1**) and independently tuning the heaters both above and below the wafer.

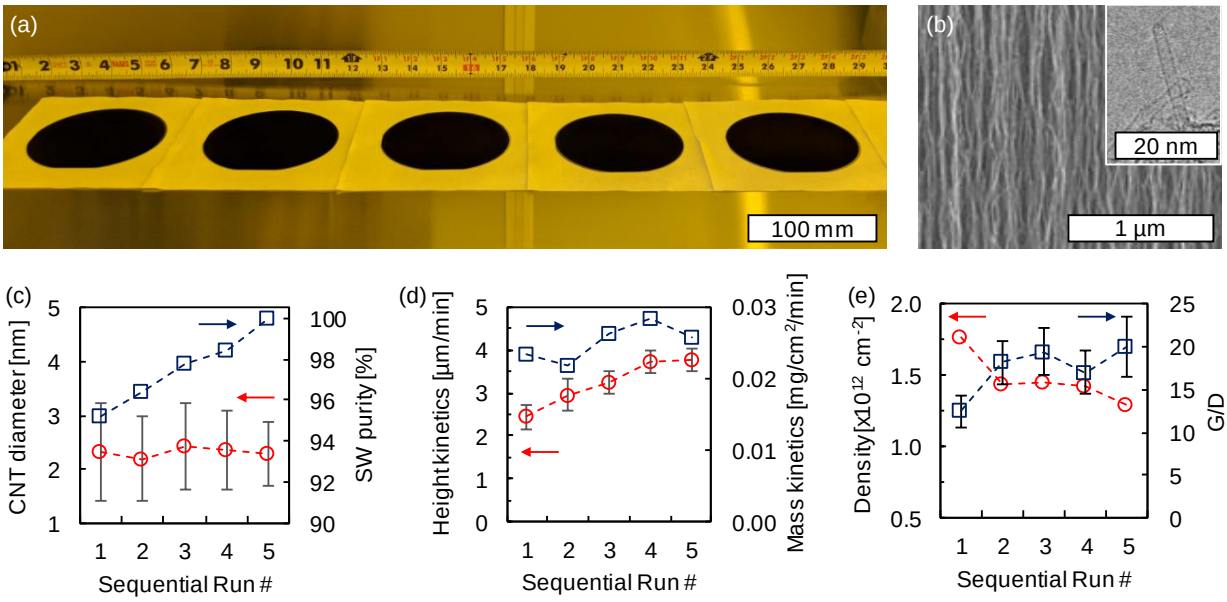

Figure 2. Five sequentially grown CNT forests on 4-in. wafers: (a) photograph of the wafers; (b) SEM image of a forest side wall with the inset showing a high-resolution TEM image of a single-walled CNT; (c) TEM measurements of the mean SWCNT diameter (error bars represent ± standard deviation of the diameter distribution at the center of the wafer) and percentage of single-walled CNTs compared to double- and triple-walled CNTs (TEM sample number $n \geq 122$); (d) SWCNT forest height kinetics (error bars represent ± standard deviation across the wafer) and mass kinetics; (e) SWCNT number density and graphitization level as measured by the Raman G/D ratio (error bars represent ± standard deviation across the wafer). Height and G/D mean and standard deviation values calculated from maps shown in **Figure S4**.

Without an optimal thermal gradient [34], we observed markedly worse growth coverage over multiple runs (**Figure S2**). Controlling H_2O vapor levels in the reactor was highlighted in several other studies as an important factor for repetition of growth results [31, 32, 35].

This set of five wafer-scale forests exhibited highly aligned morphologies comprised of small, predominantly single-walled (SW) nanotubes as shown in **Figure 2b**. The mean diameter from high-resolution TEM imaging was consistently small, only varying between 2.19 and 2.43 nm, while the SW purity maintained $\geq$ 95.2% and trended monotonically toward 100% with each sequential run (**Figure 2c**), indicating the presence of fewer larger-diameter, double-walled CNTs. On one hand, the forest height kinetics in **Figure 2d** increased monotonically with each run, from 2.4 to 3.8 μm/min (coefficient of variance, CV, across each wafer = 7-12%); on the other hand, the area-normalized mass accumulation kinetics (i.e., "mass kinetics", **Figure 2d**) appeared steadier over the five runs and did not exhibit a clear trend. Both SWCNT diameter and mass kinetics were essentially constant. Consequently, number density tracked inversely with the height kinetics, exhibiting a slight decay from 1.76×10^{12} to 1.29×10^{12} cm^{-2}. Raman spectroscopy mapping of the wafer area revealed that the integrated G/D ratio (i.e., graphitization level) trended upward with each run from ~12 to 20, although the most significant change was between the first two runs (CV $\leq$ 0.18 for all runs). The increase in G/D was consistent with the increase in SW abundance in **Figure 2c**. We also demonstrated reproducible wafer-scale growth on Fe/Al_2O_3 without Mo, and we observed largely similar trends across five runs as described in the Supporting Information (**Figure S3**). Decisive differences between Fe/Mo- and Fe-catalyzed growth are discussed in a later section.

2.2 Structural uniformity

Having established high-quality, small-diameter, and high-density SWCNT forest growth over multiple growth runs, we sought to quantify the uniformity across an individual wafer with a set of advanced characterization techniques, including Raman spectroscopy, synchrotron small-angle X-ray scattering (SAXS), and proton ion RBS. These probes generated property maps of the wafer area and enabled point-for-point correlations between multiple properties. Using the first run from the sample set described in **Figure 2**, we focused on analyzing G/D, forest height, SWCNT diameter, height and mass kinetics, and density. To our knowledge, this is the first detailed characterization mapping of wafer-scale CNT forests of any kind.

Raman spectroscopy has been used before to generate 1D scans of the structural quality and diameters of SWCNTs along the side wall of CNT forests [36] or even across wafers [22], and confocal microscopy was recently applied to generate 2D height maps of small areas [37]. While Raman microscopy has been employed to map wafer-scale graphene [38], to our knowledge, there are no reports of full-wafer mapping of SWCNT characteristics. **Figure 3a** shows Raman spectra collected at the SWCNT wafer's center as well as the resultant average from multiple points around the edges. The concavity and radial symmetry of the distribution of G/D values were evident (**Figure 3b)**, with a maximum of ~15 occurring in the center and values rolling off monotonically toward the edges. In contrast, the forest height map generated by automatic topographical tracking in **Figure 3c** illustrated the opposite concavity, with minimum values

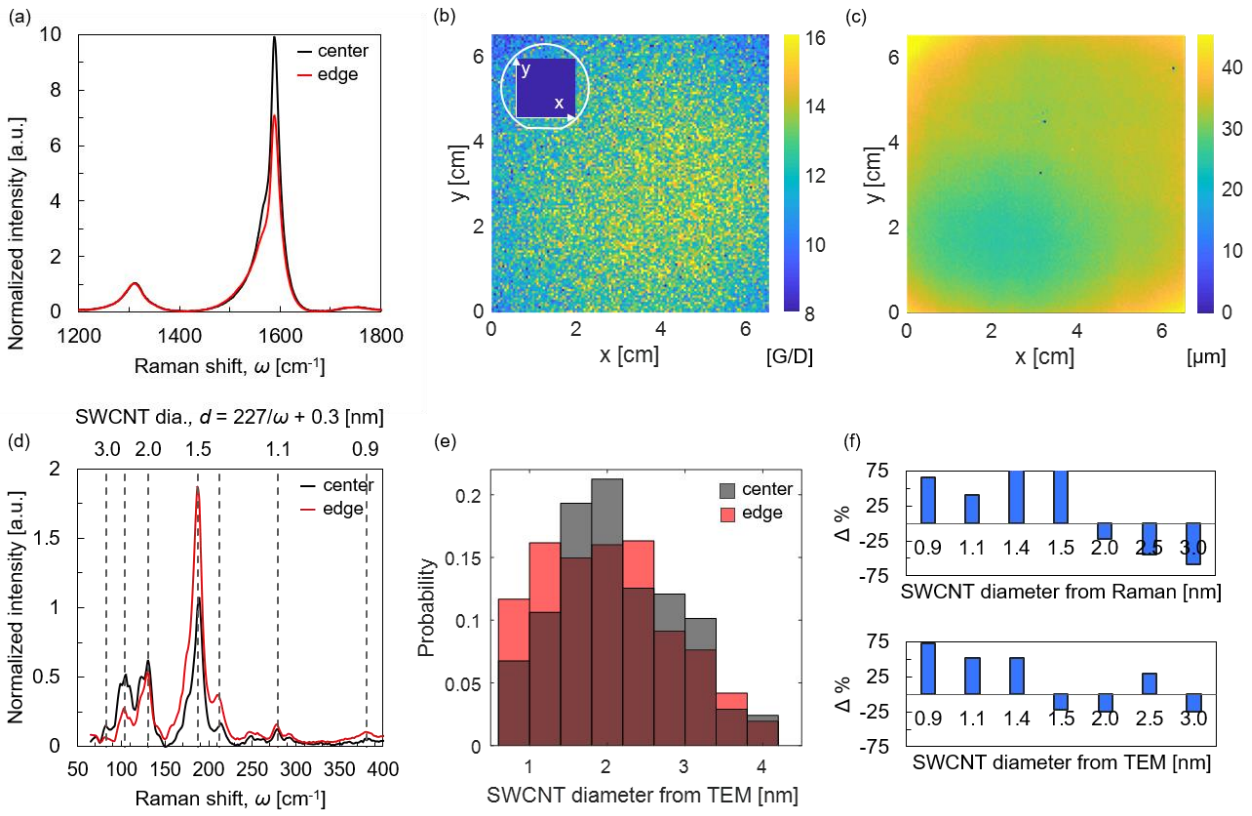

Figure 3. Raman microscopy mapping (λ = 633 nm) of the SWCNT wafer grown in the first run of **Figure 2**: (a) Representative G- and D-bands at the center and edge of the wafer (normalized to D-band); (b) G/D map of 6.5 x 6.5 cm^2 (500 μm steps) square area inscribed within the wafer (as illustrated by the inset blue square) generated by integrating the area under the peaks; (c) SWCNT forest height (stage z position at each collection point); (d) representative radial breathing modes (RBMs) at the center and edge of the wafer (normalized to D-band as in (a)), where top axis shows diameter in nm $d = 227/\omega + 0.3$ (RBM maps for several SWCNT diameters are shown in **Figure S6**); (e) TEM measurements of the SWCNT diameter at the center (mean ± standard deviation, $\mu \pm \sigma = 2.15 \pm 0.86$ nm; sample size, $n = 209$) and edge ($\mu \pm \sigma = 2.06 \pm 0.89$ nm; $n = 668$) of the wafer; (f) percent diameter change from the wafer's center extracted from Raman (top) and TEM data (bottom) for selected diameters. Same trends were observed for 514 nm and 785 nm lasers (not shown).

near the wafer's center and maxima arising at the edges. Both the general symmetry and concavity of the G/D and height maps were self-consistent over multiple growths (**Figure S4**).

The concavity of the radial breathing mode (RBM) maps was more nuanced and depended on the frequency tracked. We used the well-established relationship $d = 227/\omega + 0.3$ [39], where ω is the Raman shift in cm^{-1} and d is the SWCNT diameter in nm, to resolve multiple distinct diameters of the forest's subpopulation, namely 0.9, 1.1, 1.4, 1.5, 2.0, 2.5 and 3.0 nm. Moving from the center to the wafer edge, the RBM intensities in the normalized spectra of **Figure 3d** decrease at lower wavenumbers (larger diameters) and increase at higher wavenumbers (smaller diameters). Although RBM intensities collected from the top of the forest are not strict indicators of a specific diameter abundance, high-resolution TEM of SWCNTs harvested at several locations about the wafer corroborated this interpretation. With both analysis methods, the relative abundance of SWCNTs with a diameter less than ~1.5 nm was higher at the wafer's edge compared to the center (**Figure 3f**), which could be the result of conflated factors, such as gradients in temperature and precursor concentration from center to edge.

To complement the RBM and TEM diameter analysis, we mapped the same wafer with SAXS to extract the local mean SWCNT diameter and qualitative information regarding SW purity. SAXS was chosen to nondestructively interrogate the nano- and atomic-scale features of large populations (~10^9) of CNTs in a single shot. SAXS has previously been used to map alignment [40-42], density [43], diameter [43, 44], and wall number [43, 45] along the vertical direction of CNT forests, as well as to map a few of these structural features *in situ* during forest growth [46, 47] or across multiple length scales [48]. Still, there have been no reports of SAXS

mapping of CNT forests in the plane of the substrate to analyze lateral variations in structure, let alone across large substrate areas.

To measure SWCNT diameter, we first resolved the form factor peak in the inverse q space (**Figure 4a**), where q is the momentum transfer vector defined by $\frac{4\pi}{\lambda}\sin\theta$, λ is the incident X-ray wavelength, and θ is the scattering angle. The form factor peak contains information regarding the SWCNT diameter distribution, and we have shown previously that the characteristic length $d = \frac{2\pi}{q}$ extracted from the peak location in q corresponds well to the mean CNT diameter from TEM analysis [48]. To further validate this relationship, we calibrated SAXS experiments against TEM over a more finely resolved range of SWCNT diameters (1.51-3.72 nm), which revealed a strong linear correlation (R^2 = 0.97) between the two techniques (**Figure 4b**). In addition to the form factor peak, we previously detected a broad (002) peak at $q \approx 18$ nm^{-1} for a mixed single-walled/double-walled forest [48]. There were no such scattering peaks in this higher q range at any point on the wafer, which confirms a lack of multilayer graphitic wall structure and thus corroborated the high SW purity reported in **Figure 2c**.

Having established a fine-tuned quantitative relationship for extracting SWCNT diameter from the SAXS peak position, we mapped the mean diameter values for the same wafer described in **Figure 3** at step sizes of 1 cm with an X-ray beam width of ~0.08 cm. The SAXS mapping results in **Figure 4c** indicated a range of local, mean SWCNT diameters from 1.88 to 2.21 nm, with an average mean diameter of 2.07 ± 0.07 nm and a coefficient of variation of 0.03 across the wafer. Direct SAXS-TEM comparisons at 5 different locations across the wafer (grey

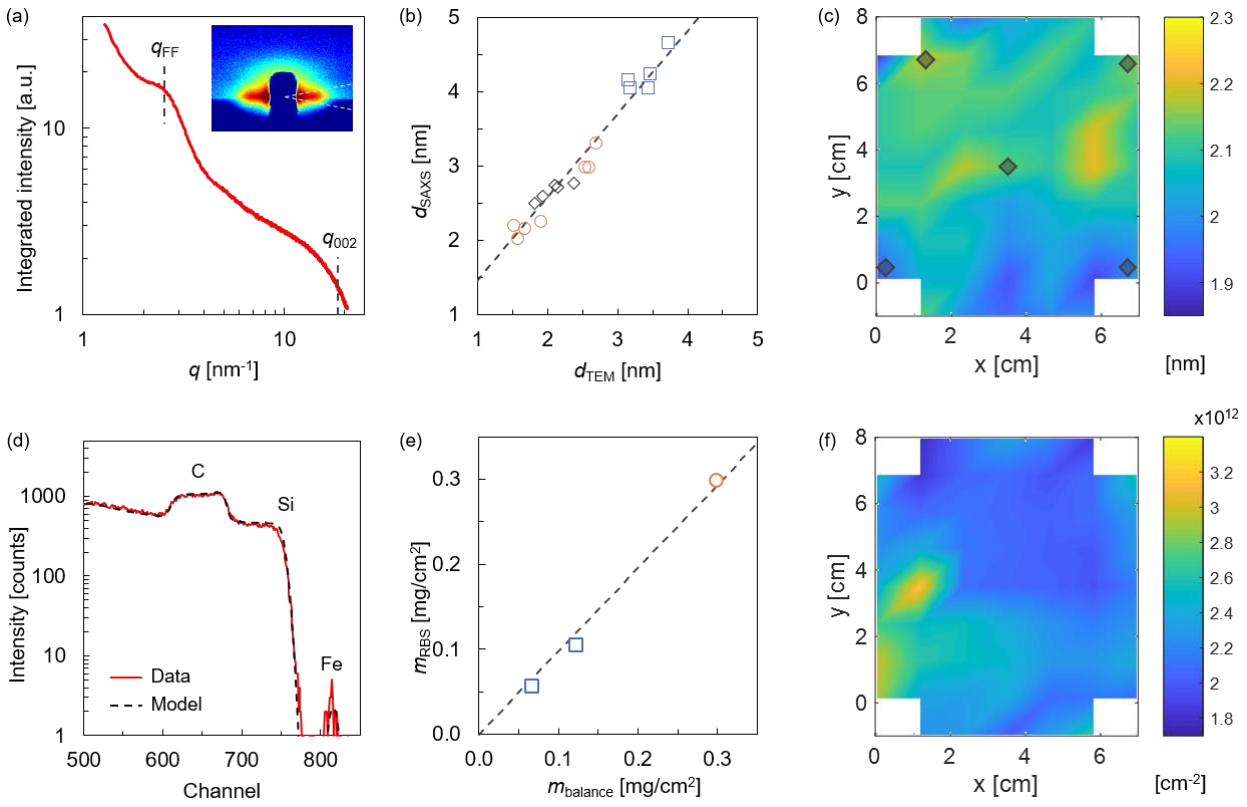

Figure 4. Diameter and density mapping the SWCNT wafer grown in the first run shown in **Figure 2**: (a) SAXS 1D $I(q)$ integrated from the sector defined by the dashed white lines in the inset 2D anisotropic scattering pattern (horizontal range corresponds to $q = \pm 6$ nm^{-1}), and two vertical dashed grey lines marking the q positions of both the form factor (FF) and the theoretical (002) ($q_{002} = 2\pi/0.34$ nm) peaks (the lack a defined peak here indicates high SW purity [43]); (b) correlation between X-ray ($d_{SAXS} = 2\pi/q_{FF}$) and TEM measurements of mean SWCNT diameter with a linear fit of the orange circles and blue squares ($d_{SAXS} = 1.12d_{TEM} + 0.34$; $R^2 = 0.97$); (c) map of SWCNT mean diameter derived from SAXS measurements calibrated by the TEM data in (b) (colorbar shown in units of nm); (d) representative RBS spectrum of a SWCNT forest (dashed line: model curve), showing the backscattering signal from the C forest and from Si and Fe underneath; (e) correlation of forest mass measured by RBS and by a balance, where RBS

data points are averaged triplicates across 1 cm^2 of a wafer-scale SWCNT forest (vertical error bars are smaller than the data points; linear fit with a slope of 0.98 and $R^2 = 0.99$); (f) map of SWCNT number density (colorbar units: 10^{12} cm^{-2}). Grey diamonds in (b) represent data collected from the four corners plus the center of the mapped area as marked in (c). In (b) and (e), orange circles represent data collected from wafer-scale SWCNT forests grown from Fe/Mo, while blue squares are from Fe only. Maps in (c) and (f) were generated by interpolating between data points collected at ~1 cm intervals in *x* and *y*. Maps of catalyst thickness, height, mass kinetics, and volumetric mass density are in **Figure S7**.

diamonds in **Figure 4c**) were consistent with the calibration curve in **Figure 4b** and confirmed the diameter trends from center to edge observed with TEM and Raman.

Ion beam analysis was recently applied to qualitatively analyze alignment and areal density in CNT forests indirectly from their hydrogen content [49]. However, we are not aware of any previous reports of direct measurements of forest density by proton ion RBS in the non-Rutherford regime or of any reports of ion beam analysis to map large CNT forest areas. To extract the areal density of carbon in our forests, we utilized spectral shifts from the Si substrate buried beneath the forest. Such a density measurement is based on the fact that the probing H ion beam experiences energy loss while passing through the CNTs so that the forest density is proportional to the energy shift of the scattering signal from the underlying Si substrate (**Figure 4d)**. We further validated our approach by comparing areal mass density values measured by both RBS and mass gained after SWCNT synthesis for a set of wafer-scale SWCNT forests grown with approximately the same height yet at widely different densities, spanning nearly an order of magnitude (**Figure 4e**). Thermogravimetric analysis (TGA) showed that the amount of lower-order carbon species in our forests is less than 5% (**Figure S8**), so the error in our CNT mass and number density calculations with both RBS and weight gain method is small.

With RBS we mapped out the areal density across the same SWCNT wafer at identical locations to those at which we performed SAXS experiments (~1 cm spacing). Incorporating the forest height measurements from our Raman analysis and the mean diameter values from SAXS, we generated the number density map of a full SWCNT wafer shown in **Figure 4f**. The mean number density was $2.26 \pm 0.27 \times 10^{12}$ cm^{-2} (CV = 0.12), and the values ranged from 1.77 to 3.17×10^{12} cm^{-2}, which proved that the density remained high for all regions of the wafer. Interestingly, the density inversely correlates with height, so the densest region of the forest

occurred around the minimum of the height map. In the next section, we further studied this tradeoff in the context of a broader library of wafer-scale forest growth results.

2.3 Global correlations

2.3.1 Diameter and density

Having established reproducible wafer-scale synthesis and mapped key structural characteristics, we focused on understanding their correlations, or lack thereof. A clear tradeoff was present in our diameter-density map (**Figure 5a**), where smaller CNT diameters are coincident with higher densities across both Fe and Fe/Mo catalysts, with Fe/Mo yielding categorically higher densities. Note that we also included data extracted from the full-wafer SAXS and RBS maps to illustrate that the constituent locations from a single wafer overlapped well with our broader sample set. Despite using the same nominal catalyst thicknesses for the entire data set (i.e., RBS measured 5.0 ± 0.4 Å of Fe and 0.4 ± 0.3 Å of Mo), we observed scatter in the diameter-density characteristics but no trend with either catalyst thickness for our Fe/Mo catalysts or the ratio between the two metals (**Figure S9**).

From this density-diameter map, we extracted a power-law dependence with an exponent of -3.7 ($R^2 = 0.78$), which translates to a steeper slope compared with close-packing and dewetting models (i.e., $N \sim d^{-2}$) [23], but it is on par with previously published results [50]. The theoretical limit of close-packed cylinders serves as a reference to illustrate that, although our material is approaching maximum density values, there is still room for decreasing diameter and

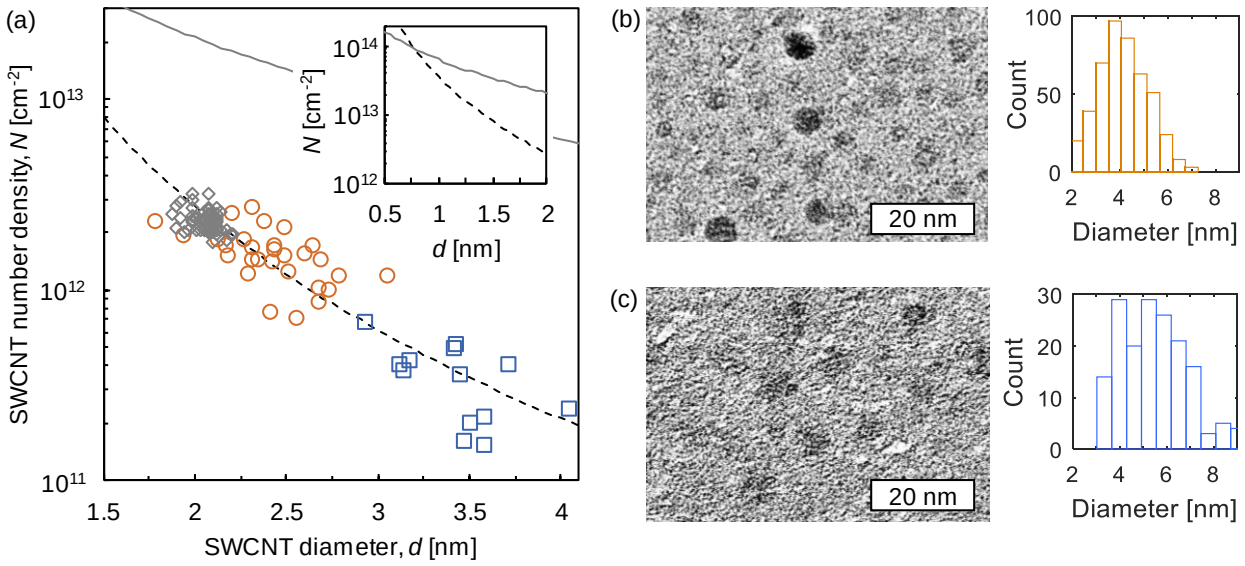

Figure 5. (a) Correlation between SWCNT diameter d and number density N. The solid grey line represents the close packing limit ($N \sim d^{-2}$), while the black dashed line is a power law fit ($N = 3.6 \times 10^{13}\ d^{-3.7}$; $R^2 = 0.78$). Inset: lower diameter limit of the two curves. Grey diamonds in (a) represent the 62 data points that define the maps in **Figure 4**, and orange circles represent average data collected from wafer-scale forests grown from Fe/Mo, while blue squares are from Fe only. TEM image analysis of (b) Fe/Mo and (c) Fe particles, showing representative planview images alongside particle diameter histograms. Fe/Mo particles were 4.1 ± 1.0 nm in diameter at a number density of 1.1×10^{12} cm^{-2} (n = 461 particles), while Fe particles were 5.4 ± 1.3 nm in diameter at 4.0×10^{11} cm^{-2} (n = 167 particles). Forests with typical Raman characteristics can be grown from these particles (see **Figure S10**). Additional TEM images are in **Figure S11**.

increasing density. Namely, extrapolating along this curve, we would reach the close-packing limit at SWCNT diameter of 0.8 nm and density of 9.1 x 10^{13} cm^{-2}.

Comparing *ex situ* TEM image analysis of the catalyst particles after annealing with the SWCNT diameter and density reveals correlations that reasonably explain the differences between Fe/Mo and Fe in **Figure 5a**. As shown by early work with Fe/Mo [51-53], particles formed in the presence of Mo are smaller (4.1 nm diameter) and more numerous (1.1 x 10^{12} cm^{-2} density) than the case without Mo (5.4 nm diameter and 4.0 x 10^{11} cm^{-2} density), even with nominally the same thickness of Fe deposited (**Figure 5b, c)**. The difference in particle diameter is similar to the difference we observe in our SWCNT diameters (~1.5 nm). The particle density values represent lower bounds because we only reported measurements for particles clearly resolved in TEM images. Additionally, the catalyst film for TEM analysis was specially prepared on silicon nitride TEM grids coated with a thinner Al_2O_3 layer (10 nm) than the Si wafers used for large-area growths (40 nm). Thus, we do not expect a one-to-one correlation with forest density, but the orders of magnitude match well. Furthermore, particles in the Fe/Mo sample appear well defined, whereas the particles in the Fe-only sample are poorly defined due to lower contrast with the support, which may suggest a difference in particle shape as well. These observations indicate that priming the Al_2O_3 surface with Mo before Fe deposition engenders topographical and/or energetic characteristics that favor smaller, more numerous particles. The importance of the interaction between Fe particles and Al_2O_3 supports for catalyst particle and resultant forest formation has been studied extensively [54, 55].

2.3.2 Kinetics and density

The differences between our two catalysts were further revealed when analyzing their wafer-scale kinetics. To ensure that termination effects (e.g., density decay) did not impact our

kinetics analyses, we performed a large set of wafer-scale syntheses with growth times more than an order of magnitude shorter than the catalyst lifetime. Uniform forests from Fe and Fe/Mo catalysts (**Figure 6a**) self-terminated abruptly at 210 min reaching terminal heights of 1.7 and 0.8 mm, respectively (**Figure 6b**), and displayed a rapid growth acceleration at the end of the growth. Despite the drastic difference in height kinetics and thus larger terminal height for Fe, these reactions remarkably converted carbon gas into SWCNT product at nearly the same rate (~0.16 mg/cm^2/min). This is consistent with our previous observation in **Figure 2d** that the mass kinetics were relatively invariant despite variations among height kinetics and density. This was further manifested over a broader sample set (**Figure 6c**), which shows that for a fixed C_2H_2 flow rate, mass kinetics exhibited no trend with height kinetics (growth time $\leq$ 15 min). This was true for several different Fe and Fe/Mo catalyst depositions, even if the height kinetics for Fe were always higher.

Across a large set of experiments shown in **Figure 6c**, the carbon conversion from the gas phase to solid SWCNT varied little and was independent of SWCNT lengthening rate, despite the 8-fold rate span from 1.6 to 13.2 μm/min. The mass kinetics did depend proportionately on the flow rate of C_2H_2, with 9 sccm and 16 sccm tested in addition to the large set grown with 4 sccm. We also included the RBS map data points to show that values across the wafer were consistent with average individual growths. Mass kinetics did not depend on the amount of metal catalyst material within the range of film thicknesses used in this study (3.7 to 6.2 Å) (**Figure S12**), nor did it track with SWCNT diameter (**Figure S13**). This lack of dependence on the catalyst type and amount may be a consequence of a growth regime limited by gas-phase processes; reactions at the catalyst particles are likely much faster, so that the overall mass kinetics are insensitive to the catalyst details.

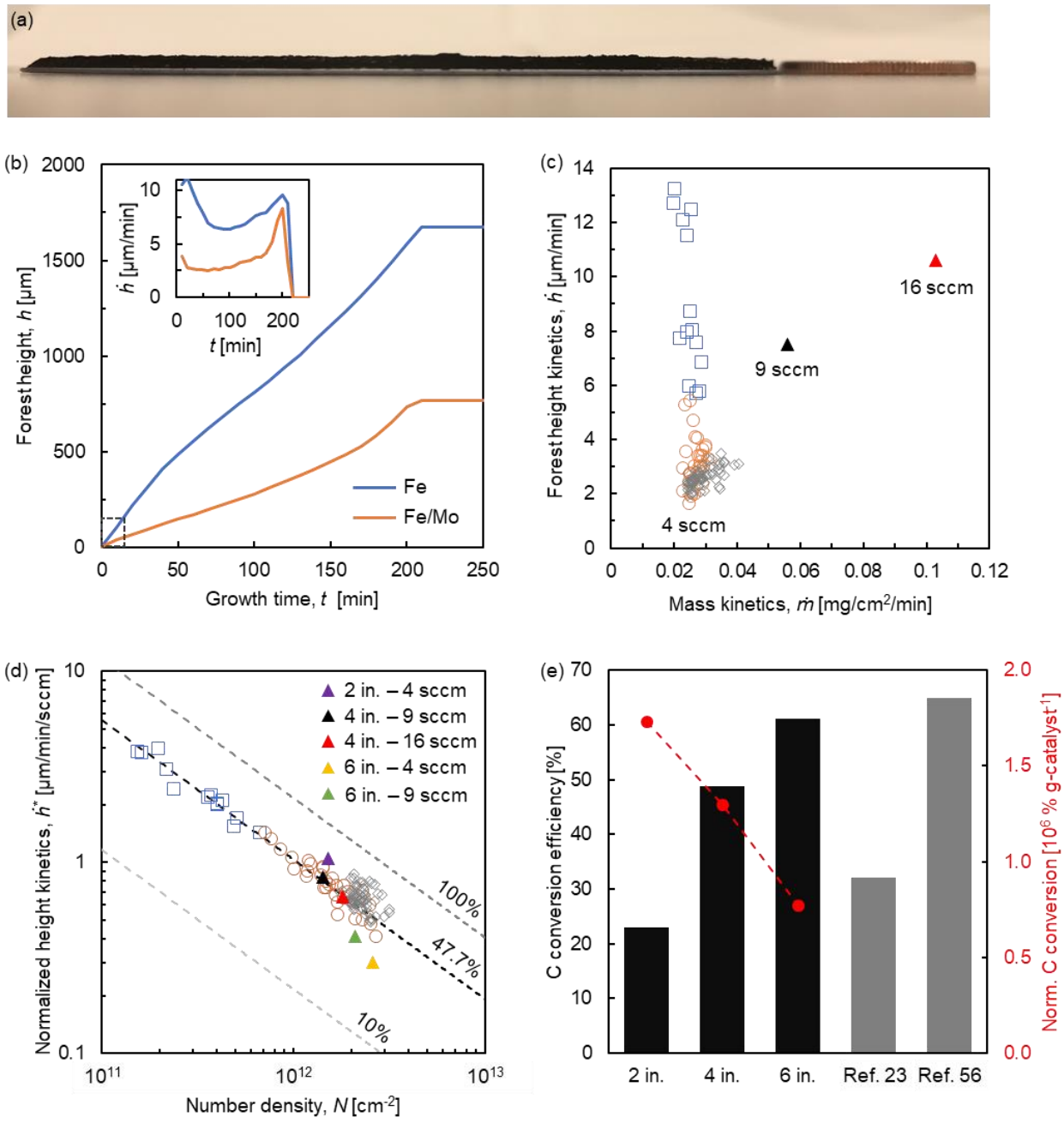

Figure 6. (a) Photograph showing a SWCNT forest grown using Fe/Mo to full termination on a 4 in. Si wafer (525 μm thick) next to a U.S. quarter coin for scale (1.75 mm thick). (b) SWCNT forest height and growth kinetics (inset) versus growth time at the center of a 4 in. wafer measured by cross-sectional SEM of witness marks created by cyclically switching C_2H_2 flow on for 10 min and off for 1 min. Dashed grey box indicates the time scale of all experiments

described in (c)-(e). Complementary experiments with smaller pulse durations were performed to verify that growth within this time window was well behaved (**Figure S14**). (c) Correlation between SWCNT forest height kinetics $\dot{h}$ and mass kinetics $\dot{m}$ for 4-in. wafer growth with 4, 9, and 16 sccm C_2H_2 flow rates. (d) Correlation between number density and forest height kinetics $\dot{h}^*$ normalized by number of walls n_w from TEM and C_2H_2 flow rate $\dot{m}_{C2H2}$ ($\dot{h}^* = \dot{h} \times n_w / \dot{m}_{C2H2}$). Different substrate sizes are displayed compared to our growth model assuming our experimentally observed 47.7% conversion (dashed black line), as well as 10% (light grey dashed line) and 100% conversion (dark grey dashed line). (e) Carbon conversion efficiency (g CNT/g carbon delivered x 100%) compared to Ref. [29] and [56] in the bar chart, along with a scatter plot of the values normalized by the mass of metal catalyst on the substrate. C_2H_2 flow rate $\dot{m}_{C2H2}$ for all experiments was 4 sccm except where otherwise noted. In (c), (d), and (e), all growth times were 3-15 min (before self-termination), grey diamonds represent the 62 data points that define the maps in **Figure 4**, and orange circles represent average data collected from wafer-scale SWCNT forests grown from Fe/Mo, while blue squares are from Fe only.

Due to the constant mass conversion rate, the height kinetics were strongly and inversely correlated with the number of SWCNTs growing in concert (**Figure 6d**), which reflects similar trends found in the literature [57]. A substrate with more catalyst particles (i.e., high density and/or large substrate) necessarily resulted in a slower elongation rate of individual SWCNTs because of the lower carbon mass available per particle. This is true even though the SWCNT diameters accompanying higher-density forests were smaller and thus required less carbon per unit length to form (**Figure S13**). Intriguingly, this rate-density coupling suggests that the widely reported density decay characteristic of the end of growth [58, 59] should manifest as an *acceleration* in height kinetics immediately preceding self-termination. This is contrary to the ubiquitous growth deceleration reported in literature, yet an acceleration is clearly reflected in our results both in **Figure 6b** and **Figure S14**. In the latter case, early self-termination ensued starting at the wafer's center first, and growth at the wafer's edge concomitantly accelerated due to newly abundant hydrocarbon precursors no longer being consumed by the self-terminated region. These various factors are all indicative of growth kinetics dominated by slow gas-phase processes that undersupply reactants to the catalyst particles, which in turn readily convert carbon upon arrival. This explains the proportional increase in mass kinetics with increased C_2H_2 flow rate, the invariant conversion efficiencies with catalyst type, and the direct interplay between accelerating and decelerating growth regions on a wafer.

To further support our claims of carbon-starved mass kinetics and density-dependent height kinetics, we built a simple growth model. The model assumes that the height kinetics of the entire forest are equivalent to the lengthening rate of a single CNT and proportional to the rate of carbon delivered to an individual catalyst particle. Neglecting tortuosity has minimal

effect in our study since tortuosity is expected to be high or varying only in very low-density and/or self-terminated forests, respectively [41]. The expression of forest height kinetics is

$$\dot{h} = \frac{SSA_G}{\pi d}\dot{m}_{\mathrm{CNT}}. \quad (1)$$

Here, SSA_G is the specific surface area of graphene (1315 m^2/g), d is the CNT diameter, and $\dot{m}_{\mathrm{CNT}}$ is the rate of carbon mass incorporation into the CNT. From the fitted power-law relationship in **Figure 5a**, we can rewrite d in terms of number density N such that $d \propto N^{-\alpha}$, where α= 1/3.7. Furthermore, $\dot{m}_{\mathrm{CNT}}$ is related to C_2H_2 flow rate into the reactor, $\dot{m}_{\mathrm{C2H2}}$, by $\dot{m}_{\mathrm{CNT}} = \varepsilon \frac{\dot{m}_{\mathrm{C2H2}}}{A \cdot N}$, where A is the growth substrate area, and ε is the carbon conversion efficiency from the gas to solid phase, which encompasses several factors, including effects of chamber geometry and residence time, gas decomposition, and catalyst efficiency (with the last factor being inconsequential for the growths of this study). Thus, we recover a power-law dependence between height kinetics and number density, $\dot{h} \propto N^{1-\alpha}$, where the proportionality depends on ε/A and $\dot{m}_{\mathrm{C2H2}}$, as shown in **Figure S15**. Increasing either parameter effectively allows more carbon to reach the growing SWCNT and thus increased the height kinetics for the otherwise same density. We calculated the average value of ε from mass kinetics data (47.7%) for our large 4-in. data set, and we readily know $\dot{m}_{\mathrm{C2H2}}$ based on the flow rate we use in our recipe.

Overlaying this model calculated for a 4-in. wafer on our experimental results in **Figure 6d** showed good agreement over the extensive data range. To allow comparison on a single plot between different C_2H_2 flow rates, we normalized the height kinetics by C_2H_2 flux and obtained a master curve for a specific ε/A along which all our experiments fell. In particular, the

normalized height kinetics for 4-in. growth from 9 and 16 sccm C_2H_2 lie on the master curve as anticipated by our model. We also performed additional experiments with different sized substrates, and we observed that smaller substrates lied above, while wafers larger than 4 in. lied below the master curve (ε/A trends described in **Figure S15**). As shown in **Figure 6e,** this trend is linked to a decline in area-normalized conversion efficiency with increasing growth substrate size. Interestingly, local areas on the fully mapped wafer may be highly efficient (e.g., grey diamonds reaching as high as 74%).

2.4 Implications for scale-up

The conclusions of this study offer three significant implications for designing and scaling up growth of small-diameter, high-density SWCNT forests. First, operating in a carbon-starved regime enables a carbon conversion efficiency that far exceeds typical benchtop reactor processes [60] and is on par with the best reported literature values. As illustrated in **Figure 6e**, the current work outperforms the highest values for gas-showerhead SWCNT forest growth [29] and is comparable to fluidized-bed growth of small-diameter CNT forests [61, 62]. Carbon conversion efficiency at 4 in. (6 in.) was constant among the three C_2H_2 flow rates tested on Fe/Mo, with a mean of 47.1± 1.7 % (64.3 ± 4.5%), or accounting for the amount of catalyst available in the reactor, 1.24 ± 0.04 x $\times 10^6$ % g-catalyst^{-1} (0.80 ± 0.05 x $\times 10^6$ % g-catalyst^{-1}). A resource-efficient process is desirable for scale up to reduce both direct costs of consumables as well as indirect costs due to environmental impacts (e.g., unnecessarily exhausting greenhouse gases). Time is also an important factor determining efficiency and scalability of a synthesis process. Although the growth rate in our carbon-starved regime is not as high as in yield-optimized supergrowth processes [29], our results demonstrate growth kinetics at constant

conversion efficiency that are widely tunable by adjusting C_2H_2 flow rates and nanotube density. Knowledge gained in this low-pressure study could be transferred to higher-pressure regimes to accelerate the process. Incidentally, increasing C_2H_2 did not significantly change the SWCNT diameter or graphitization (**Figure S16**), which is likely the result of operating in the carbon-starved growth regime. Previous reports showed that increasing C_2H_2 resulted in higher SWCNT forest density [23], but we did not observe such an enhancement. Thus, C_2H_2 flow rate is a convenient tuning parameter to scale forest growth rates without altering the forest characteristics.

Second, the addition of Mo is critical for achieving uniform growth of smaller, denser SWCNTs. It has been previously shown in literature that the addition of Mo to Fe in the range of 6-10 at.% can enhance SWCNT growth in several ways, such as by a) increasing catalytic activity [51, 63], b) inhibiting deleterious Fe oxide and carbide formation [64, 65], and c) creating smaller and denser particles [51]. Contrary to early reports [63], our experiments in **Figure 6c** did not show enhanced carbon conversion efficiency for Fe/Mo over Fe only ($1.28 \pm 0.11 \times 10^6$ versus $1.33 \pm 0.15 \times 10^6$ % g-catalyst^{-1}, respectively). Although we do not have direct evidence of the chemical state of the particle, our long growth experiments in **Figure 6b** self-terminated at the same time for Fe and Fe/Mo. The fact that Mo did not extend the reaction lifetime or the carbon conversion over the course of a prolonged 3.5-hour growth suggests that either oxide/carbide phases did not contribute to self-termination, or the presence of Mo simply did not inhibit the formation of these phases. As in previous reports [51-53], we did observe smaller, denser particles with the presence of Mo (**Figure 5b, c**), which shows adding Mo to Fe provides one potential path for scaling diameter/density characteristics toward the close-packing limit.

Third, we deciphered a master analytical relationship between SWCNT forest yield versus density that is independent of the catalyst details and can be used to guide growth on silicon substrates (**Figure 6d**) and scale up on even larger metal foils (**Figure 1**) [27]. The insensitivity in growth performance to catalyst chemical composition is likely a direct consequence of a growth regime dominated by slow gas-phase processes, which renders the nanotube synthesis more robust and reproducible by mitigating the impact of possible catalyst variations from batch to batch. In this regime, the forest height kinetics scale proportionally with the carbon gas input and inversely with the total number of SWCNTs in the reactor (i.e., number density × substrate area). This enables prediction of how to tune recipes to meet target growth rates and how to scale trial growth experiments on small substrates up to large wafers or beyond. Increasing the substrate size increased the absolute carbon conversion, yet the conversion did not scale proportionally with area, which underlines an important practical consideration in optimal reactor design with respect to the substrate's area. Dedicated follow-on studies will be targeted at determining quantitative relationships between conversion efficiency, substrate size, and process parameters such as C_2H_2 concentration and chamber pressure.

3. Conclusion

We achieved the first demonstration of uniform and repeatable growth of small-diameter and high-density SWCNT forests at wafer-scale. Furthermore, with a combination of characterization techniques, we quantified the wafer-scale uniformity of key structural features, thus providing a so-far lacking and much needed detailed analysis of large-area nanotube synthesis. Our sub-nm Fe/Mo thin films enabled growth of forests with 2.1 nm mean diameter and 2.26 x 10^{12} cm^{-2} density on up to 6-in. wafers from a dilute C_2H_2 feedstock at carbon

conversion efficiencies surpassing previous low-pressure and/or showerhead CVD processes. Furthermore, operating in a carbon-starved kinetic regime, we demonstrated that our carbon conversion rate was proportional to C_2H_2 flow rate and invariant with catalyst type. Consequently, forest height kinetics and density were inversely correlated and follow the same scaling for both Fe and Fe/Mo. In this sense, the predominant role of Mo in our study deviated from previous reports that suggested Mo enhanced catalytic performance via hydrocarbon decomposition. However, high-resolution TEM provided visual and statistical confirmation that Fe/Mo on Al_2O_3 forms particles that are smaller and denser than Fe alone, which is consistent with the prevailing literature. Together with providing readily transferable information to wafer-scale batch synthesis for electronics applications, this work is expected to help future efforts toward continuous, roll-to-roll growth of high-density, small diameters SWCNTs on even larger-area metal foils.

4. Methods

4.1 Carbon nanotube synthesis

Carbon nanotube forests were synthesized from an Fe/Mo/Al_2O_3 multilayer, thin-film catalyst. Each layer was sequentially deposited onto Si (100) wafers by electron-beam evaporation without breaking vacuum between layers (base pressure ≤ 1.6 x 10^{-6} mbar). Nominal thicknesses of the catalyst layers used in this study (Fe/Mo/Al_2O_3 = 5.5/0.5/400 Å) were recorded *in situ* by a quartz crystal monitor during deposition and subsequently confirmed *ex situ* by Rutherford backscattering spectroscopy (RBS).

We performed low-pressure chemical vapor deposition (CVD) in a cold-wall furnace (AIXTRON® Black Magic Pro 6 in.), featuring a wafer-scale, local heater stage and a gas showerhead. The chamber was pumped down below 0.2 mbar prior to initiating the growth recipe, which began with a thermal annealing step in a reducing environment before introducing the hydrocarbon feedstock growth gas (C_2H_2). For this study, we utilized the following protocol: ramp temperature at 200-300 °C min^{-1} to 800 °C at 80 mbar in H_2/Ar = 700/200 sccm and hold for 2 min at 800 °C before switching the gas mixture to C_2H_2/H_2/Ar = 4/700/(400-x) sccm at 80 mbar for 13 min. The addition of x sccm Ar through a bubbler containing H_2O resulted in ~170-1500 ppm_v depending on x. We optimized conditions for Fe and Fe/Mo such that the Ar flow through the bubbler was fixed at 80 sccm and 20 sccm, respectively. The top heater was not required for Fe, whereas it was set to 700 °C for Fe/Mo (**Figure S2**).

The mean number density N (cm^{-2}) was measured by mass gain as described in the literature [25]. Briefly, the CNT volumetric mass density ρ was first quantified from the mass increase of the substrate after CNT growth. To get volume, the forest height was measured by optical

microscopy at 9 locations across the wafer and the area was calculated from the nominal wafer diameter.

Then number density was calculated by

$$N = \frac{\rho}{\pi d / SSA_{\mathrm{G}}}, \quad (2)$$

where d is the mean SWCNT diameter measured by TEM, and SSA_{G} is the specific surface area of graphene, 1315 $m^2 g^{-1}$. For forests with mixtures of single- and double-walled, we used a weighted aggregate diameter to account for the extra carbon in the proportion of double-walled CNTs. We have shown previously that this method agrees well with other complementary methods for density measurement, such as X-ray attenuation [16].

4.2 Rutherford backscattering spectroscopy (RBS)

RBS measurements were performed at room temperature (4 MV ion accelerator, NEC, model 4UH) to obtain areal densities of: (a) Fe and Mo in pristine catalyst films prior to CNT synthesis using 2 MeV $^4He^+$ ions and (b) CNT forests after synthesis using 2 MeV $^1H^+$ ions. The ion beam (with 2 mm spot size) was incident normal to the sample surface and backscattered into a detector at 164° relative to the incident beam direction. Analysis of RBS spectra was done with stopping powers and scattering cross sections from the SIMNRA code [66].

4.3 X-ray characterization experiments

We conducted synchrotron X-ray scattering at the Advanced Light Source using beamline 7.3.3 with a 1475 x 1679 Dectrus Pilatus 2M pixel array detector and a fixed 10 keV incident energy and beamspot 250 μm tall and 800 μm wide [67]. Labview automated the stage translation, sample alignment to the beam, and image collection, which enabled fast screening of

the entire 4-in. wafer. A custom MATLAB script was used to reduce and analyze scattering data.

4.4 Microscopy

High-resolution transmission electron microscopy (HRTEM) was used to quantify catalyst particle size distributions and number density, CNT diameter distributions, and CNT wall number n_w, each with a sample number $N \geq 100$ (image processing performed using a custom MATLAB script). We used a JEOL 2100-F field-emission analytical TEM, operating at 200 kV. For particle preparation, we deposited by e-beam evaporation our nominal Fe/Mo and Fe thicknesses on 10 nm Al_2O_3, all deposited on silicon nitride TEM membranes 10 nm thick. We annealed the catalyst films according to our standard process in the AIXTRON tool and cooled the chamber under vacuum. For CNT preparation, we dispersed CNT forests in ethanol with ultrasonication and subsequently dropcasting the dispersion onto Cu TEM grids coated with Formvar. We defined the diameter of a SWCNT as the perpendicular distance from the center of one wall to the center of the other. Scanning electron microscopy (SEM) was performed with a Thermo Scientific Apreo SEM, operated at 5 kV accelerating voltage, with the incident electron beam perpendicular to the CNT axis.

4.5 Raman spectroscopy

Micro-Raman spectroscopy was performed using an inVia™ Qontor® confocal Raman microscope with excitation wavelength of λ = 633 nm at 20 mW power, a 1200 lines/mm grating, and a 50x long working distance objective magnification for ~ 1 μm spotsize. Mapping was performed using LiveTrack™ to automatically track the top surface of the forest on a 6.5 cm

square area inscribed within the circular forest area with 500 μm steps (17161 total points collected in 160 min). Maps were collected with 10% power and 0.5-second exposure at each spot, while single point spectra (i.e., **Figure 3a, d**) where collected with 5% power and 5-second exposure averaged over 5 accumulations. Each spectrum was baseline subtracted with an 11^{th} order polynomial prior to data analysis. We quantified the mean structural quality of our CNT by calculating the ratio between the peak areas of the D-band (~1310 cm^{-1}) and G-band (~1590 cm^{-1}), and the radial breathing mode peak intensities were extracted by integrating the area under the peak and normalizing to the D-band peak area.

ACKNOWLEDGEMENT

This work is supported by the Defense Threat Reduction Agency (DTRA) D[MS]^2 project under Contract No. BA12PHM123. The work was performed under the auspices of the U.S. Department of Energy by the Lawrence Livermore National Laboratory under Contract DE-AC52-07NA27344. The Advanced Light Source and the Molecular Foundry are both supported by the Office of Science, Office of Basic Energy Sciences, of the U.S. Department of Energy under Contract No. DE-AC02-05CH11231. The authors are grateful for assistance from Alex Liebman-Pelaez and Chenhui Zhu with X-ray scattering, Supakit Charnvanichborikarn with RBS measurements and analysis, Rahul Rao with supplementary Raman measurements, and Shaul Aloni with TEM imaging.

ASSOCIATED CONTENT

Supporting Information

H_2O vapor optimization results; statistics of wafer-scale growth success with top heating; wafer-scale sequential growth from Fe catalyst; wafer-scale maps of G/D ratio, forest height, RBMs, Fe thickness, mass kinetics, areal mass density, volumetric mass density of wafer grown from Fe/Mo; validation of forest height maps with optical microscopy; thermogravimetric analysis (TGA); SWCNT diameter, density, versus catalyst thickness and Mo/Fe ratio; verification of forest growth on TEM membranes with photographs and Raman analysis; additional TEM images of catalyst particles; mass kinetics versus total catalyst thickness; mass and height kinetics versus SWCNT diameter; SWCNT forest height versus growth time for a

successful and failed growth; growth model for height kinetics versus number density as it depends on C_2H_2 flow rate, efficiency, density-diameter scaling and substrate area; G/D ratio, SWNT diameters and densities as a function of C_2H_2 flow rate.

REFERENCES

[1] Chiodarelli N, Li Y, Cott DJ, Mertens S, Peys N, Heyns M, et al. Integration and electrical characterization of carbon nanotube via interconnects. Microelectron Eng. 2011;88(5):837-43.

[2] Xie R, Zhang C, van der Veen MH, Arstila K, Hantschel T, Chen B, et al. Carbon nanotube growth for through silicon via application. Nanotechnology. 2013;24(12):125603.

[3] Vahdani Moghaddam M, Yaghoobi P, Sawatzky GA, Nojeh A. Photon-Impenetrable, Electron-Permeable: The Carbon Nanotube Forest as a Medium for Multiphoton Thermal-Photoemission. ACS Nano. 2015;9(4):4064-9.

[4] Perea-López N, Rebollo-Plata B, Briones-León JA, Morelos-Gómez A, Hernández-Cruz D, Hirata GA, et al. Millimeter-Long Carbon Nanotubes: Outstanding Electron-Emitting Sources. ACS Nano. 2011;5(6):5072-7.

[5] Theocharous E, Chunnilall CJ, Mole R, Gibbs D, Fox N, Shang N, et al. The partial space qualification of a vertically aligned carbon nanotube coating on aluminium substrates for EO applications. Opt Express. 2014;22(6):7290-307.

[6] Titova LV, Pint CL, Zhang Q, Hauge RH, Kono J, Hegmann FA. Generation of Terahertz Radiation by Optical Excitation of Aligned Carbon Nanotubes. Nano Lett. 2015;15(5):3267-72.

[7] Ren L, Pint CL, Arikawa T, Takeya K, Kawayama I, Tonouchi M, et al. Broadband Terahertz Polarizers with Ideal Performance Based on Aligned Carbon Nanotube Stacks. Nano Lett. 2012;12(2):787-90.

[8] He X, Fujimura N, Lloyd JM, Erickson KJ, Talin AA, Zhang Q, et al. Carbon Nanotube Terahertz Detector. Nano Lett. 2014;14(7):3953-8.

[9] Sharma A, Singh V, Bougher TL, Cola BA. A carbon nanotube optical rectenna. Nat Nano. 2015;10(12):1027-32.

[10] Taphouse JH, Smith ONL, Marder SR, Cola BA. A Pyrenylpropyl Phosphonic Acid Surface Modifier for Mitigating the Thermal Resistance of Carbon Nanotube Contacts. Adv Funct Mater. 2014;24(4):465-71.

[11] Nuri Na and Kei Hasegawa and Xiaosong Zhou and Mizuhisa Nihei and Suguru N. Denser and taller carbon nanotube arrays on Cu foils useable as thermal interface materials. Japanese Journal of Applied Physics. 2015;54(9):095102.

[12] Kaur S, Raravikar N, Helms BA, Prasher R, Ogletree DF. Enhanced thermal transport at covalently functionalized carbon nanotube array interfaces. 2014;5:3082.

[13] Xu M, Du F, Ganguli S, Roy A, Dai L. Carbon nanotube dry adhesives with temperature-enhanced adhesion over a large temperature range. 2016;7:13450.

[14] Thevamaran R, Meshot ER, Daraio C. Shock formation and rate effects in impacted carbon nanotube foams. Carbon. 2015;84:390-8.

[15] Ozden S, Tiwary CS, Hart AHC, Chipara AC, Romero-Aburto R, Rodrigues M-TF, et al. Density Variant Carbon Nanotube Interconnected Solids. Adv Mater. 2015;27(11):1842-50.

[16] Bui N, Meshot ER, Kim S, Peña J, Gibson PW, Wu KJ, et al. Ultrabreathable and Protective Membranes with Sub-5 nm Carbon Nanotube Pores. Adv Mater. 2016;28(28):5871-7.

[17] Wu J, Gerstandt K, Zhang H, Liu J, Hinds BJ. Electrophoretically induced aqueous flow through single-walled carbon nanotube membranes. Nat Nano. 2012;7:133-9.

[18] Wu J, Paudel KS, Strasinger C, Hammell D, Stinchcomb AL, Hinds BJ. Programmable transdermal drug delivery of nicotine using carbon nanotube membranes. Proc Natl Acad Sci U S A. 2010;107(26):11698-702.

[19] Fornasiero F, Park HG, Holt JK, Stadermann M, Grigoropoulos CP, Noy A, et al. Ion exclusion by sub-2-nm carbon nanotube pores. Proc Natl Acad Sci U S A. 2008;105(45):17250-5.

[20] Jiang K, Wang J, Li Q, Liu L, Liu C, Fan S. Superaligned Carbon Nanotube Arrays, Films, and Yarns: A Road to Applications. Adv Mater. 2011;23(9):1154-61.

[21] Liang Y, Sias D, Chen PJ, Tawfick S. Tough Nano-Architectured Conductive Textile Made by Capillary Splicing of Carbon Nanotubes. Advanced Engineering Materials. 2017:1600845-n/a.

[22] Wyss RM, Klare JE, Park HG, Noy A, Bakajin O, Lulevich V. Water-Assisted Growth of Uniform 100 mm Diameter SWCNT Arrays. ACS Applied Materials & Interfaces. 2014;6(23):21019-25.

[23] Zhong G, Warner JH, Fouquet M, Robertson AW, Chen B, Robertson J. Growth of Ultrahigh Density Single-Walled Carbon Nanotube Forests by Improved Catalyst Design. ACS Nano. 2012;6(4):2893-903.

[24] Esconjauregui S, Fouquet M, Bayer B, Ducati C, Smajda R, Hofmann S, et al. Growth of Ultrahigh Density Vertically Aligned Carbon Nanotube Forests for Interconnects. Acs Nano. 2010;4(12):7431-6.

[25] Esconjauregui S, Xie R, Fouquet M, Cartwright R, Hardeman D, Yang J, et al. Measurement of area density of vertically aligned carbon nanotube forests by the weight-gain method. Journal of Applied Physics. 2013;113(14):144309-7.

[26] Cui K, Kumamoto A, Xiang R, An H, Wang B, Inoue T, et al. Synthesis of subnanometer-diameter vertically aligned single-walled carbon nanotubes with copper-anchored cobalt catalysts. Nanoscale. 2016;8(3):1608-17.

[27] Zhong G, Yang J, Sugime H, Rao R, Zhao J, Liu D, et al. Growth of high quality, high density single-walled carbon nanotube forests on copper foils. Carbon. 2016;98:624-32.

[28] Suguru Noda and Hisashi Sugime and Kei Hasegawa and Kazunori Kakehi and Yosuke S. A Simple Combinatorial Method Aiding Research on Single-Walled Carbon Nanotube Growth on Substrates. Japanese Journal of Applied Physics. 2010;49(2S):02BA.

[29] Yasuda S, Futaba DN, Yamada T, Satou J, Shibuya A, Takai H, et al. Improved and Large Area Single-Walled Carbon Nanotube Forest Growth by Controlling the Gas Flow Direction. ACS Nano. 2009;3(12):4164-70.

[30] World's First Super-Growth Carbon Nanotube Mass Production Plant Opens. 2015 [cited; Available from: http://www.zeon.co.jp/press_e/151104.html

[31] Stadermann M, Sherlock SP, In J-B, Fornasiero F, Park HG, Artyukhin AB, et al. Mechanism and Kinetics of Growth Termination in Controlled Chemical Vapor Deposition Growth of Multiwall Carbon Nanotube Arrays. Nano Letters. 2009;9(2):738-44.

[32] Oliver CR, Polsen ES, Meshot ER, Tawfick S, Park SJ, Bedewy M, et al. Statistical Analysis of Variation in Laboratory Growth of Carbon Nanotube Forests and Recommendations for Improved Consistency. ACS Nano. 2013;7(4):3565-80.

[33] Li J, Bedewy M, White AO, Polsen ES, Tawfick S, Hart AJ. Highly Consistent Atmospheric Pressure Synthesis of Carbon Nanotube Forests by Mitigation of Moisture Transients. The Journal of Physical Chemistry C. 2016;120(20):11277-87.

[34] Youn SK, Frouzakis CE, Gopi BP, Robertson J, Teo KBK, Park HG. Temperature gradient chemical vapor deposition of vertically aligned carbon nanotubes. Carbon. 2013;54:343-52.

[35] Lee J, Abdulhafez M, Bedewy M. Data Analytics Enables Significant Improvement of Robustness in Chemical Vapor Deposition of Carbon Nanotubes Based on Vacuum Baking. Industrial & Engineering Chemistry Research. 2019;58(27):11999-2009.

[36] Hasegawa K, Noda S. Millimeter-Tall Single-Walled Carbon Nanotubes Rapidly Grown with and without Water. Acs Nano. 2011;5(2):975-84.

[37] Piwko M, Althues H, Schumm B, Kaskel S. Confocal Microscopy for Process Monitoring and Wide-Area Height Determination of Vertically-Aligned Carbon Nanotube Forests. Coatings. 2015;5(3):477-87.

[38] Tian M, Hu B, Yang H, Tang C, Wang M, Gao Q, et al. Wafer Scale Mapping and Statistical Analysis of Radio Frequency Characteristics in Highly Uniform CVD Graphene Transistors. Advanced Electronic Materials. 2019;0(0):1800711.

[39] Araujo PT, Maciel IO, Pesce PBC, Pimenta MA, Doorn SK, Qian H, et al. Nature of the constant factor in the relation between radial breathing mode frequency and tube diameter for single-wall carbon nanotubes. Physical Review B. 2008;77(24):241403.

[40] Meshot ER, Hart AJ. Abrupt self-termination of vertically aligned carbon nanotube growth. Applied Physics Letters. 2008;92(11):113107.

[41] Meshot E, Bedewy M, Lyons K, Woll A, Juggernauth K, Tawfick S, et al. Measuring the lengthening kinetics of aligned nanostructures by spatiotemporal correlation of height and orientation. Nanoscale. 2010:896-900.

[42] Vainio U, Schnoor TIW, Koyiloth Vayalil S, Schulte K, Müller M, Lilleodden ET. Orientation Distribution of Vertically Aligned Multiwalled Carbon Nanotubes. The Journal of Physical Chemistry C. 2014;118(18):9507-13.

[43] Bedewy M, Meshot ER, Reinker MJ, Hart AJ. Population Growth Dynamics of Carbon Nanotubes. Acs Nano. 2011;5(11):8974-89.

[44] Bedewy M, Meshot ER, Hart AJ. Diameter-dependent kinetics of activation and deactivation in carbon nanotube population growth. Carbon. 2012;50(14):5106-16.

[45] Furuta H, Kawaharamura T, Furuta M, Kawabata K, Hirao T, Komukai T, et al. Crystal Structure Analysis of Multiwalled Carbon Nanotube Forests by Newly Developed Cross-Sectional X-ray Diffraction Measurement. Applied Physics Express. 2010;3(10).

[46] Meshot ER, Verploegen E, Bedewy M, Tawfick S, Woll AR, Green KS, et al. High-Speed in Situ X-ray Scattering of Carbon Nanotube Film Nucleation and Self-Organization. ACS Nano. 2012.

[47] Landois P, Pinault M, Rouzière S, Porterat D, Mocuta C, Elkaim E, et al. In situ time resolved wide angle X-ray diffraction study of nanotube carpet growth: Nature of catalyst particles and progressive nanotube alignment. Carbon. 2015;87:246-56.

[48] Meshot ER, Zwissler DW, Bui N, Kuykendall TR, Wang C, Hexemer A, et al. Quantifying the Hierarchical Order in Self-Aligned Carbon Nanotubes from Atomic to Micrometer Scale. ACS Nano. 2017;11(6):5405-16.

[49] Girshevitz O, Richter V, Avraham ES, Nessim GD, Gouzman I. Correlation between density and hydrogen content in vertically aligned carbon nanotube forests by ion beam analysis. Journal of Vacuum Science & Technology A. 2017;35(6):061403.

[50] Sakurai S, Inaguma M, Futaba DN, Yumura M, Hata K. Diameter and Density Control of Single-Walled Carbon Nanotube Forests by Modulating Ostwald Ripening through Decoupling the Catalyst Formation and Growth Processes. Small. 2013;9(21):3584-92.

[51] Ago H, Uehara N, Yoshihara N, Tsuji M, Yumura M, Tomonaga N, et al. Gas analysis of the CVD process for high yield growth of carbon nanotubes over metal-supported catalysts. Carbon. 2006;44(14):2912-8.

[52] Youn SK, Park HG. Morphological Evolution of Fe–Mo Bimetallic Catalysts for Diameter and Density Modulation of Vertically Aligned Carbon Nanotubes. The Journal of Physical Chemistry C. 2013;117(36):18657-65.

[53] Pint CL, Nicholas N, Pheasant ST, Duque JG, Parra-Vasquez ANG, Eres G, et al. Temperature and Gas Pressure Effects in Vertically Aligned Carbon Nanotube Growth from Fe−Mo Catalyst. The Journal of Physical Chemistry C. 2008;112(36):14041-51.

[54] Mattevi C, Wirth CT, Hofmann S, Blume R, Cantoro M, Ducati C, et al. In-situ X-ray photoelectron spectroscopy study of catalyst-support interactions and growth of carbon nanotube forests. Journal of Physical Chemistry C. 2008;112(32):12207-13.

[55] Amama PB, Pint CL, Kim SM, McJilton L, Eyink KG, Stach EA, et al. Influence of Alumina Type on the Evolution and Activity of Alumina-Supported Fe Catalysts in Single-Walled Carbon Nanotube Carpet Growth. ACS Nano. 2010;4(2):895-904.

[56] Kim DY, Sugime H, Hasegawa K, Osawa T, Noda S. Fluidized-bed synthesis of sub-millimeter-long single walled carbon nanotube arrays. Carbon. 2012;50(4):1538-45.

[57] Zhang C, Xie R, Chen B, Yang J, Zhong G, Robertson J. High density carbon nanotube growth using a plasma pretreated catalyst. Carbon. 2013;53:339-45.

[58] Bedewy M, Meshot E, Guo H, Verploegen E, Lu W, Hart A. Collective Mechanism for the Evolution and Self-Termination of Vertically Aligned Carbon Nanotube Growth. Journal of Physical Chemistry C. 2009;113(48):20576-82.

[59] Amama P, Pint C, McJilton L, Kim S, Stach E, Murray P, et al. Role of Water in Super Growth of Single-Walled Carbon Nanotube Carpets. Nano Lett. 2009;9(1):44-9.

[60] Shi W, Xue K, Meshot ER, Plata DL. The carbon nanotube formation parameter space: data mining and mechanistic understanding for efficient resource use. Green Chemistry. 2017;19(16):3787-800.

[61] Chen Z, Kim DY, Hasegawa K, Osawa T, Noda S. Over 99.6wt%-pure, sub-millimeter-long carbon nanotubes realized by fluidized-bed with careful control of the catalyst and carbon feeds. Carbon. 2014;80:339-50.

[62] Kim DY, Sugime H, Hasegawa K, Osawa T, Noda S. Sub-millimeter-long carbon nanotubes repeatedly grown on and separated from ceramic beads in a single fluidized bed reactor. Carbon. 2011;49(6):1972-9.

[63] Mora E, Harutyunyan AR. Study of Single-Walled Carbon Nanotubes Growth via the Catalyst Lifetime. The Journal of Physical Chemistry C. 2008;112(13):4805-12.

[64] Yoshida H, Shimizu T, Uchiyama T, Kohno H, Homma Y, Takeda S. Atomic-Scale Analysis on the Role of Molybdenum in Iron-Catalyzed Carbon Nanotube Growth. Nano Letters. 2009;9(11):3810-5.

[65] Curtarolo S, Awasthi N, Setyawan W, Jiang A, Bolton K, Tokune T, et al. Influence of Mo on the Fe:Mo:C nanocatalyst thermodynamics for single-walled carbon nanotube growth. Physical Review B. 2008;78(5):054105.

[66] Doolittle LR. Algorithms for the rapid simulation of Rutherford backscattering spectra. Nuclear Instruments and Methods in Physics Research Section B: Beam Interactions with Materials and Atoms. 1985;9(3):344-51.

[67] Hexemer A, Bras W, Glossinger J, Schaible E, Gann E, Kirian R, et al. A SAXS/WAXS/GISAXS Beamline with Multilayer Monochromator. Journal of Physics: Conference Series. 2010;247:012007.